DOI: 10.13009/EUCASS2023-005
Aerospace Europe Conference 2023 – 10TH EUCASS – 9TH CEAS

Setup of flight experiment of transpiration cooled sharp edge fins on the sounding rocket HIFLIER1

Giuseppe Di Martino, Jonas Peichl*†, Fabian Hufgard**, Christian Duernhofer**, Stefan Loehle***

** DLR Institute of Structures and Design, Pfaffenwaldring 38-40, 70569 Stuttgart, Germany*

*** High Enthalpy Flow Diagnostics Group, Institute of Space Systems, University of Stuttgart Pfaffenwaldring 29, 70569 Stuttgart, Germany*

† Corresponding Author – E-mail: Jonas.Peichl@dlr.de

Abstract

The flight in hypersonic conditions implies important challenges for the vehicle development concerning the thermal protection of the external structures, especially in the case of sharp leading edges, where the short standoff distance of the forming shock waves typically determines severe aero-thermal loads. In the framework of the HIFLIER1 flight research experiment, the DLR Institute of Structures and Design, in collaboration with the High Enthalpy Flow Diagnostics Group at the University of Stuttgart, is responsible for setting up the so-called FinExII module of the sounding rocket, for flight testing of the transpiration cooling technology applied to porous ceramic matrix composite structures as a possible approach for thermal management of sharp leading edges in hypersonic regime. For this purpose, the module will house four fins, whose leading edge is made of an inhouse-developed porous C/C-SiC material, connected to a gas system feeding nitrogen for the transpiration cooling application. The present paper gives an overview of the module design, supported by efficient numerical modelling to estimate the effect of the transpiration cooling, and the pre-flight activities, including the fins manufacturing and pre-flight characterization as well as the rocket module setup.

1. Introduction

The flight in hypersonic conditions implies important challenges for the vehicle development concerning especially the thermal protection of the external structures, which are exposed to the actual high enthalpy flow field, resulting in high thermal loads on the vehicle structure. In the cases of sharp leading edges, like for example for wing leading edges, stabilizer fins and air intakes, the high heat loads become even more critical, because the strong shock is not detached from the surface as it is the case for blunt bodies [1].

Since the 1990s, lightweight ceramic matrix composites (CMC), such as C/C-SiC, are of fundamental interest as thermal protection systems due to their high temperature resistance and favourable thermal and mechanical properties. However, the material is challenging in terms of design and manufacturing. In this framework, the Institute of Structures and Design of the German Aerospace Centre (DLR-BT) has developed a unique expertise for the development of such materials [2], its full characterization as well as the integration and validation as a thermal protection system (TPS) for hypersonic sounding rocket flight experiments, successfully flown for example in SHEFEX I and II [3, 4] and most recently in STORT [5, 6]. The FinEx experiment on the HiFire-5 flight experiment [7] proved the successful implementation of this material for stabilizer fin structures.

In order to overcome the load limits for sharp leading edges, active cooling of the structure could become necessary, e.g. for flight at increasing Mach number or for longer operational time, i.e. for increasing integral thermal load. In this framework, one of the possibilities is represented by transpiration cooling, which consists in forcing a coolant fluid through a porous wall into the hot gas region, with the double effect of directly cooling the wall itself and mixing into the boundary layer creating a protective cooling film resulting in a lower convective heat flux [8, 9].

In order to combine the application of CMC structures with the transpiration cooling technology, DLR-BT has worked in the past years in the development of a variant of the C/C-SiC material with defined porosity level designed specifically for transpiration cooling applications, denominated OCTRA (Optimized Ceramic for Hypersonic Application with Transpiration Cooling) [10]. OCTRA has only been used so far in ground testing experiments of a sharp leading edge design [11], as well as in the context of investigating rocket engine combustion chamber cooling [12].

In order to test the mentioned technologies applied to stabilizing fins with sharp leading edge under real hypersonic flight conditions, the DLR-BT, in collaboration with the High Enthalpy Flow Diagnostic group (HEFDiG) of the Institute of Space Systems (IRS) at the University of Stuttgart is responsible for the design and construction of a sounding rocket module (so called FinExII). The module will be hosted on the sounding rocket developed in the

DOI: 10.13009/EUCASS2023-005

framework of the Hypersonic International Flight Research Experimentation (HIFLIER1), a project coordinated by the US Air Force Research Laboratory (AFRL) in collaboration with DLR's Mobile Rocket Base (MORABA) for the management of the flight mission campaign. The flight of the sounding rocket is scheduled in October 2023.
In the present paper, the FinExII module design will be presented. The design process is supported by numerical analyses for the estimation and verification of the fins' thermo-structural behaviour and for a first qualitative evaluation of the heat transfer reduction on the fins due to transpiration cooling and the corresponding temperatures. The manufacturing process of the CMC fins, the assembly of the rocket module and the preliminary ground tests carried out for the calibration and verification of the experimental concept, from the characterization of the permeability of the fin leading edges to the calibration of the coolant gas system operating conditions, will also be described.

2. FinExII design overview

The general design of the sounding rocket module dedicated to the FinExII experiment is shown in Figure 1.

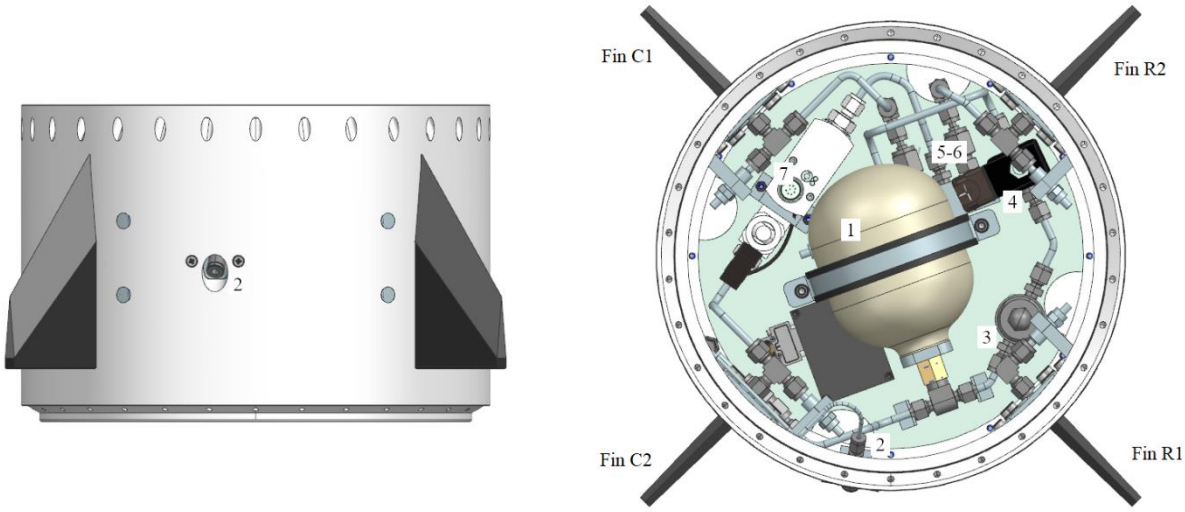

Figure 1: FinEx II module overall design.

In particular, the module is equipped with four identical fins as shown in Figure 1, each pair of diametrically opposite fins exposed to the same flow conditions determined by the upstream sounding rocket forebody.
A detailed description of the fins design, the gas system configuration and the operating conditions is given in the following.

2.1 Design of the CMC fins with porous leading edge for transpiration cooling

Figure 2 shows a schematic of the fin design
.

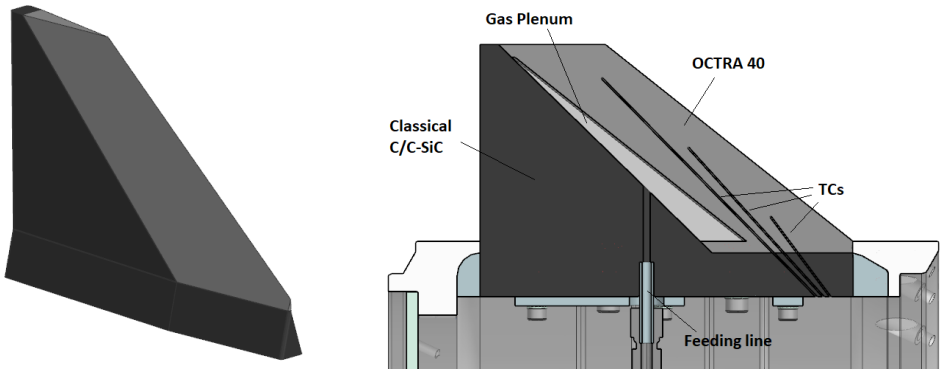

a) Fin isometric view b) Cut view of the fin integrated in the module

Figure 2: Fin design.

DOI: 10.13009/EUCASS2023-005

The fin is made of two different parts joined together. In fact, in order to concentrate the transpiration cooling in the region of the leading edge, which is expected to reach higher temperatures, only the forward part of the fin (displayed in light grey in Figure 2) is made of the permeable OCTRA material, while the remaining part (in dark grey in Figure 2) is made of classical impermeable C/C-SiC.
In particular, the OCTRA material is a development based on the C/C-SiC material obtained through the classical Liquid Silicon Infiltration (LSI) process [2], where in the initial manufacturing of the carbon fibre reinforced polymer (CFRP) precursor a defined portion of the carbon fibres is replaced with thermally non-stable aramid fibres. The fibres are degrading in the pyrolysis process step, leading to defined cavities inside the material, which cannot be completely filled in the final infiltration of liquid silicon. This allows for adjustable porosities in a range between 1% and 10% for the OCTRA material [10]. In this work, the so-called OCTRA40 material is used, indicating a 40%vol percentage of aramid fibres in the CFRP preform leading to a porosity of around 10% in the final C/C-SiC state.
The above described process allows also a control on the main orientation of the pores in the final OCTRA material and consequently of the cooling flow. In fact, using two-dimensional mixed carbon/aramid fibre plies in the manufacturing of the CFRP preform results in a main orientation of the pores parallel to the chosen fibre orientation, which for the case of the fins in the present work is shown in Figure 3.
The characterization of the base OCTRA material used in the present work is reported in [12, 13] in terms of thermophysical properties and of the Darcy-Forchheimer permeability.

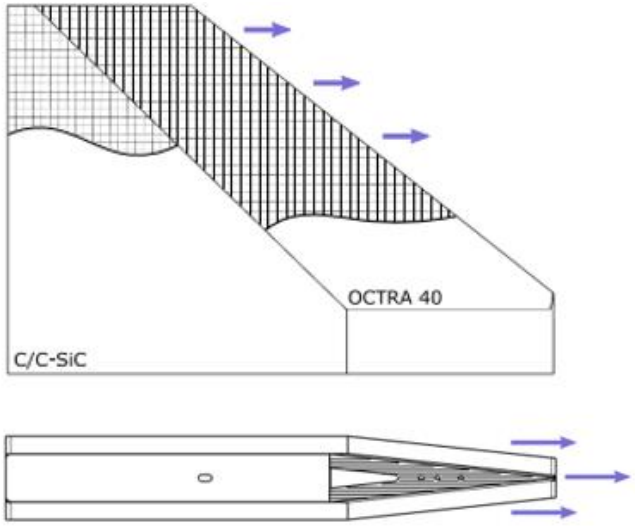

Figure 3: Fin fibres orientation.

With reference to Figure 2b, inside the permeable leading edge, a plenum volume for the cooling gas is foreseen. The gaseous nitrogen is fed in the plenum through a hole in the C/C-SiC component in which a 6 mm stainless steel tube is soldered, which assures also the sealing at the operating pressure. Three holes are included in the OCTRA40 leading edge for the routing of type K thermocouples for temperature measurements. The position of the thermocouples was defined for optimizing the inverse estimation of the wall heat flux, according to the methodology described in Sec. 2.4.

2.2 Cooling gas feeding system and nominal operation conditions

Figure 4 shows the schematic representation of the feeding line for the gaseous nitrogen employed as coolant gas. The corresponding components in the 3D CAD model, as designed for the FinEx II experiment module, can be seen in Figure 1b.
The gas is contained at an initial pressure of 240 bar in a small gas tank (ARMOTECH, 1), which has an internal volume of 800 ml. The filling of the tank is carried out before flight through the filling line (2), including a dedicated intake valve, a Swagelok® filter to avoid any contamination of the gas in the system and a check valve.
A pressure reducer (Swagelok®, 3) set to a specific position before flight reduces the gas pressure to the nominal absolute pressure of 13,7 bar defined for the transpiration cooling. The pressure reducer is followed by the solenoid valve (Bürkert 6013, 4), which is opened via an electric signal during the prescribed experiment windows.
After the solenoid valve the gas is split in two different lines through a dedicated component (5). At this point a combined pressure and temperature sensor (Kulite® HKL-T-312) is foreseen for measuring the gas total pressure and temperature.

DOI: 10.13009/EUCASS2023-005

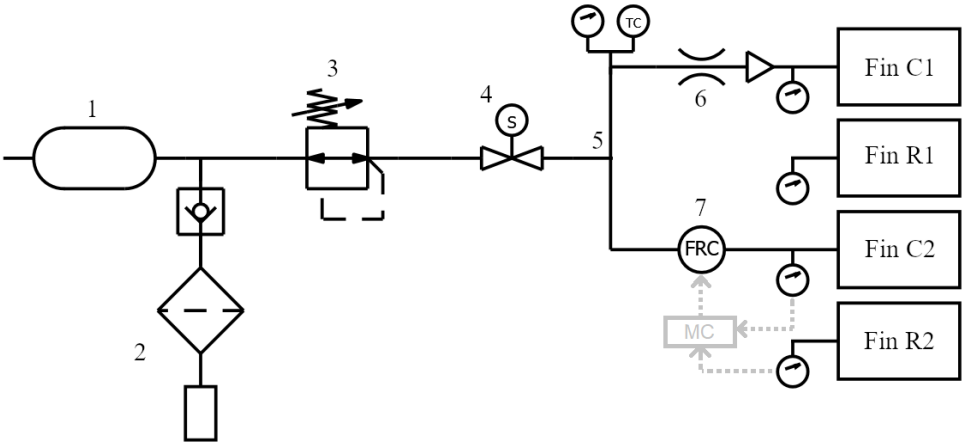

Figure 4: FinEx cooling gas feeding line schematic.

Along the line feeding the cooling gas to the Fin C1 a constant mass flow rate of the cooling gas is foreseen, which is obtained including along the line a disk with an orifice (6) with a prescribed diameter operating in choked conditions (M=1 at the throat section). On the other line feeding the cooling gas to the Fin C2, a mass flow rate controller (Bronkhorst® IN-FLOW F-201AI, 7) is included, which is in turn connected to the electronics designed to control the mass flow rate of the cooling gas according to the aerothermal load acting on the corresponding fin, as it will be described in Sec. 2.3.
Combined pressure and temperature sensor are included upstream each fin to measures the corresponding pressure and temperature in the plenum. In this way, the case of the fins R1 and R2, the pressure of the aerodynamic flow on the external surface will be obtained.
Table 1 summarizes the nominal transpiration cooling operating conditions for the different fins. For the fin C1 a traditional approach is implemented with a constant mass flow rate of the coolant gas, whose nominal value is defined based on the experience gained in the previous flight experiment AKTiV on SHEFEX II [14]. For the fin C2 a new approach is considered in which the mass flow rate of the cooling gas is adjusted in real time according to the instantaneous actual thermal load applying the so-called Cooling Adjustment for Transpiration Systems (CATS) method, developed by HEFDiG [15]; more details are given in Sec 2.3.
The transpiration cooling experiment will be activated on the two cooled fins switching on the coolant mass flow in two different time windows, with a duration of 50 s each, when hypersonic conditions (with Mach numbers up to 6) are reached during the ascent and the descent phases of the rocket flight trajectory, i.e. correspondingly to the peak of the convective heat flux, as it will be shown in Sec. 3.

Table 1: Transpiration cooling operating mass flow rates for the different fins.

Fin R1	Fin C1	Fin R2	Fin C2
No cooling Reference for fin C1	0,85 g/s	No cooling Reference for fin C2	CATS method

2.3 Cooling Adjustment for Transpiration Systems applied to FinEx II

Cooling Adjustment for Transpiration Systems (CATS) is a method to automatically adjust the cooling of a transpiration cooled wall depending on the real-time measured surface heat flux [15]. One particular feature of CATS is that the heat flux is derived from exclusively non-intrusive measurements. Hence, the transpiration cooled structure is not required to be equipped with any sensor system, which potentially weakens the structure or perturbates the transpiration cooling itself.
As shown in Figure 4, the CATS system consists of the porous fin, a mass flow rate controller and a pressure gauge to measure the pressure in the plenum, i.e. between flow controller and fin. Additionally, the plenum of the uncooled Fin R2 is equipped with a pressure gauge to measure the ambient pressure. The in-flight calculations and automatic adjustment of the cooling are performed by a microcontroller in an on-board electronics box.
The essential measurement is the pressure drop over the transpiration cooled wall. From this we find the mean fluid temperature in the transpiration cooled wall T with the relation of Darcy's law:

DOI: 10.13009/EUCASS2023-005

$$\mu(t)\,T(t) = \frac{p_{pl}^2(t) - p_a^2(t)}{2\,L}\,\frac{K\,A}{\dot{m}(t)\,R} \tag{1}$$

using a look-up table and the approximation of the viscosity by Sutherland's Law. Here, p_{pl} and p_a are the gas pressures in the plenum and the ambient, R is the specific gas constant of an ideal gas of nitrogen, L and A are the length and cross-sectional area of the porous wall and K is the permeability coefficient. The mass flow rate $\dot{m}$ is measured by the flow controller. This formulation is derived from the Darcy law with the density substituted by the ideal gas law and the superficial Darcy velocity substituted with Eq. (13).
The calculated temperature and mass flow rate are the input variables in the equation to determine the surface heat flux, which is

$$\dot{q}(t) = a\,\frac{dT(t)}{dt} + c\,\dot{m}(t)\,(T(t) - T(0)) \tag{2}$$

The parameters a and c are found using a system identification approach and non-destructive calibration of the actual flight hardware. Here, the calibration heat flux is provided by an infra-red laser.
The required calculations are computationally cheap and are performed by a microcontroller in real-time. The micro-controller adjusts the setpoint of the mass flow controller depending on the measured heat flux according to

$$\dot{m}_{set}(t) = \dot{m}_{min} + k\,\dot{q}(t) \tag{3}$$

with the minimum mass flow rate $\dot{m}_{min}$ and the proportional factor k. This means that the cooling is boosted at the same time as the heat flux affects the surface. This is particularly useful with regards to the film cooling characteristics of transpiration cooling, which reduces the inbound heat flux proportionally to its magnitude. Thus, the integrated heat load is minimized.

2.4 Non-Integer System Identification method for spatially resolved heat flux determination

The Non-Integer System Identification (NISI) Method is used for the determination of surface heat flux from an in-depth temperature measurement [16]. The process chain of the NISI method is summarized in Figure 5. A system identification approach is applied where the heat flux $\dot{q}$ and temperature T are related by

$$\sum_{n=L_0}^{L} \alpha_n \frac{d^{n/2}}{dt^{n/2}} T(t) = \sum_{n=M_0}^{M} \beta_n \frac{d^{n/2}}{dt^{n/2}} \dot{q}(t) \tag{4}$$

The parameters $\alpha_n$and β_n are found from calibration data. The actual hardware is calibrated non-destructively using an infra-red laser as the heat source.
With the identified system we calculate the system's impulse response. The impulse response is used in the final stage to solve the inverse heat conduction problem, i.e. the determination of the surface heat flux from the measured temperature data, applying common methods as for example the future time algorithm by Beck [17].
This approach can be extended to a set of temperature sensors in order to resolve the determination of surface heat flux into individual areas [18]. We apply this NISI3D approach to the HIFLIER1 fins, where we will measure the heat flux onto three areas as shown in Figure 6. The temperatures are measured by three thermocouples in each fin (see Figure 2). The experimental calibration stage is summarized in section 4.3.

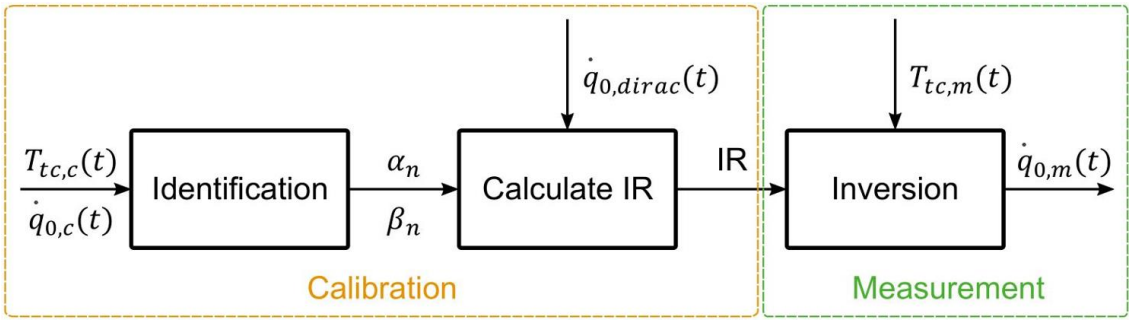

Figure 5: Flow chart of the NISI method.

DOI: 10.13009/EUCASS2023-005

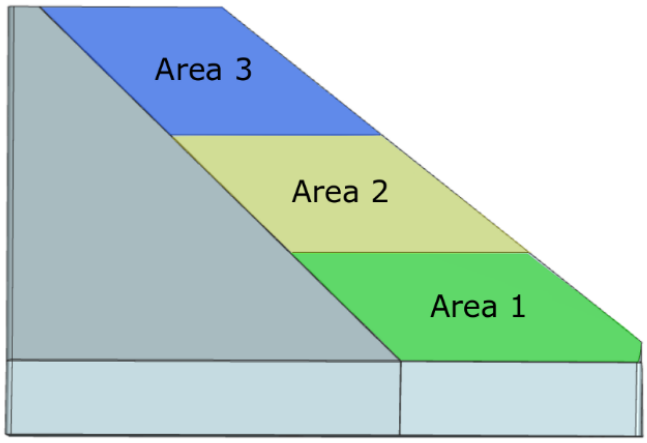

Figure 6: Discretization of fin (adapted from [19])

3. Transient thermal analyses during the flight trajectory

3.1 Numerical model

A numerical analysis of the CMC fin was performed with a simplified approach to have a relatively fast estimation of the material thermal response during the flight and the corresponding effect of activating the transpiration cooling during the chosen experimental windows.
In particular, the ANSYS Mechanical software was used to solve the transient energy equation with the Finite Element (FE) technique, At this stage, including only the fin in the calculation, considering different material properties for the OCTRA leading edge and the backward part made of classical C/C-SiC. The considered material properties can be found in Refs. [13]. The heat conduction from the fin to the module through the contact surface at the fin bottom was assessed to be negligible for the objectives of the present work.
The assigned boundary conditions include:

- a convective heat flux on the fin external surface;
- a radiative heat flux from the fin external surface exposed to the ambient, considering for the CMC material an emissivity of 0,85;
- adiabatic condition on the other surfaces.

For what concerns the estimation of the convective heat flux $\dot{q}_c$ during the flight trajectory the classical equation applies

$$\dot{q}_c = h(T_r - T_w) \tag{5}$$

where h is the heat transfer coefficient, T_r the recovery boundary-layer temperature and T_w the wall temperature.
For the sake of simplicity, in the estimation of the convective heat flux, the fin external surface was split in two parts: the external surface of the leading edge, which has a semi-angle of inclination respect to the upcoming flow of 6° (assuming null angle of attack), and the surface of the backward part which is again parallel to the flow. For each of them constant conditions are assumed. In particular, when supersonic flight is reached, the local flow conditions for the leading edge are assumed to be the conditions downstream the shock waves forming in correspondence of the trajectory conditions at each instant, while a following Prandtl-Meyer expansion is assumed for estimating the flow conditions on the backward part.
With these assumptions the heat transfer coefficient can be calculated as

$$h = St_{fl}\, c_{p,fl}\, \rho_{fl}\, V_{fl} \tag{6}$$

where the index "fl" indicates that the quantities are referred to the local external flow conditions.
The Stanton number St can be calculated with the classical correlation formula for laminar flow over a flat plat as

$$St_{fl} = 0{,}664\, Pr_{fl}^{-\frac{2}{3}}\, Re_{L,fl}^{-\frac{1}{2}} \tag{7}$$

The recovery boundary-layer temperature on the other hand is calculated as

DOI: 10.13009/EUCASS2023-005

$$T_r = T_\infty \left(1 + \sqrt{Pr_\infty}\frac{\gamma - 1}{2} M_\infty^2\right) \tag{8}$$

Finally, the wall temperature is also initially unknown. For this reason, the following iterative procedure is needed. A first trial convective heat flux is calculated with Eqs. (5) to (8) in cold wall condition, i.e. for $T_w = 298{,}15$ K. The transient thermal simulation is performed in ANSYS with the trial convective heat flux as boundary condition. From the results of the thermal simulation the time profiles of the wall temperature averaged on each surface is obtained, which then allows to calculate a new trial convective heat flux. This procedure is then iterated until the maximum relative error of the wall temperature between one step and the previous one is smaller than 5%.

3.2 Modification of the Stanton number for the case of transpiration cooling

The reduction of the heat transfer due to transpiration cooling is modelled using the correlation of Kays et al. [8], which is based on a Couette flow assumption. In the case of activation of the transpiration cooling with a fixed cooling gas mass flow rate $\dot{m}_c$ on the surface of area A_c the blowing ratio F can be defined as

$$F = \frac{\dot{m}_c}{\rho_{fl} V_{fl} A_c} \tag{9}$$

and a blowing parameter can be defined as

$$b_h = \frac{F}{St_{nc}} \tag{10}$$

where the index “nc” refers to the corresponding non-cooled case.
The Stanton number in the case with transpiration cooling can be obtained from the following equation

$$\frac{St_c}{St_{nc}} = \frac{b_h \left(\frac{c_{p,c}}{c_{p,fl}}\right)^{0,6}}{\exp\left(b_h \left(\frac{c_{p,c}}{c_{p,fl}}\right)^{0,6}\right) - 1} \tag{11}$$

where $c_{p,c}$ is the specific heat of the cooling gas.
Finally, the heat absorbed by conduction by the cooling gas is considered to be a second-order effect in the present case and is therefore neglected.

3.3 Numerical result of the fin thermal response during flight trajectory

The converged results of the described numerical model are shown in the following considering the nominal trajectory data and for the cases without cooling and with cooling with a coolant mass flow rate of 0,4 g/s and 0,85 g/s (nominal case for the fin C1). In the last two cases, the transpiration cooling is considered to be activated in the two chosen experimental windows, i.e. during ascent between +5 s and +65 s after lift-off and during descent from +365 s until landing.
Figure 7 shows the profiles of the convective heat flux on the fin leading edge-region for the considered cases, while Figure 8 shows the corresponding profiles of the minimum, maximum and average temperature (the last is used in Eq. (5)) on the surface of the same region. It can be observed that for the given ballistic trajectory, the heat flux and correspondingly the temperature reaches a peak twice, when the maximum Mach number (around 6) is reached during ascent and during descent. For this reason, the abovementioned time windows were selected for the activation of the transpiration cooling. The latter is expected to determine a significant reduction of the convective heat flux on the interested zone. With respect to the maximum value during ascent a reduction of around 40% for the case of 0,4 g/s of coolant and of around 65% for the case of 0,85 g/s of coolant can be expected, while during descent the reduction is around 20% and 50% respectively.

DOI: 10.13009/EUCASS2023-005

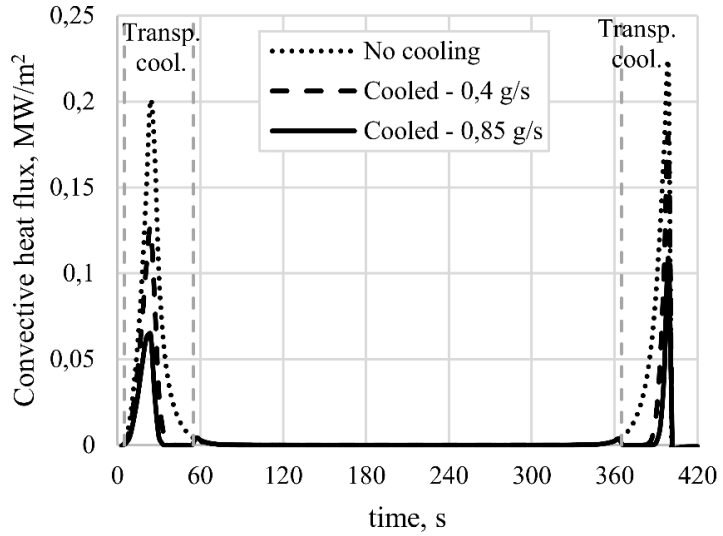

Figure 7: Comparison between the calculated time profile of the convective heat flux on the leading-edge region of the fin during the flight nominal trajectory.

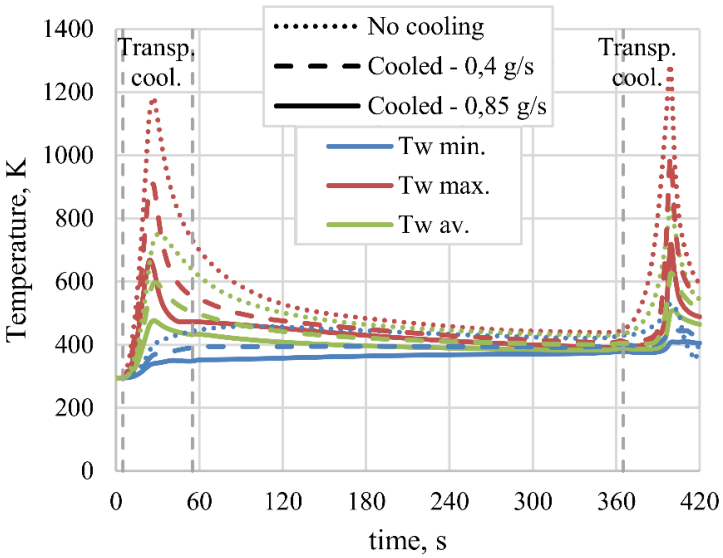

Figure 8: Comparison between the calculated time profile of the minimum, maximum and average temperature on the fin during the flight nominal trajectory.

For the sake of completeness, the temperature distribution on the fin surface for $t = 24$ s and $t = 399$ s, i.e. for the two peaks of the heat flux and temperatures during ascent and descent, are shown in Figure 9.

At this point it is worth to highlight the simplifying hypothesis of the present model, in which a uniform convective heat flux is assumed on the whole leading edge area of the fin and, in the case of transpiration cooling, a uniform coolant mass flux is assumed on the interested area as well, although the actual coolant mass flux distribution depends on the local conditions, such as the local pressure of the aerodynamic flow, the local solid temperature, as well as on the geometry of the fin (distance between the internal plenum and the external surface) and on the actual pore distribution in the material. The development of a more detailed numerical model, based on the CFD model defined in Peichl et al. [20] for the simulation of the transpiration cooling applied to internal flows, is currently ongoing. In this regard, the data collected during the flight will be of fundamental importance for the numerical model tuning and final validation.

DOI: 10.13009/EUCASS2023-005

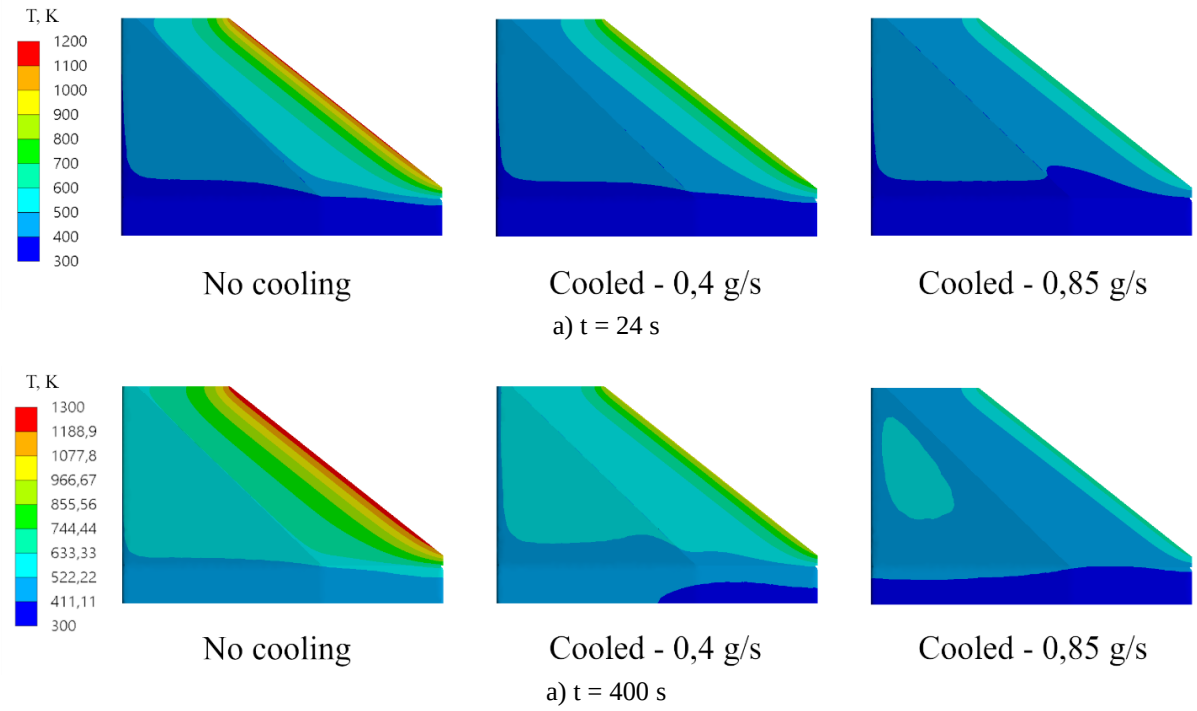

Figure 9: Comparison between the calculated fin temperature distribution in correspondence of the two peaks of maximum temperature during ascent and during descent.

4. Setup of the FinExII module

4.1 CMC fins manufacturing process

As already mentioned, the CMC fins were manufactured with the LSI method [2]. In the present case, for the backward component of the fin a material plate is manufactured via hot pressing method and pyrolyzed to the C/C status. In parallel, for the porous leading edge a plate is manufactured also with the hot-pressing method but using fabric plies with carbon and aramid fibres, as also mentioned in Sec. 2.1. The pyrolysis of this plate generates the C/C plate with a higher porosity which is the basis material for the manufacturing of the OCTRA40 component.
The two plates in the C/C status are then cut according to the transversal profile of the fin, i.e. following the geometry shown in Figure 2b for the two different part, and the plenum volume is milled in the leading edge part.
At this point the two individual parts are joined together, using a dedicated tool to allow the application of the needed pressure on the joining area and the correct relative alignment of the parts in the process, as shown in Figure 10.

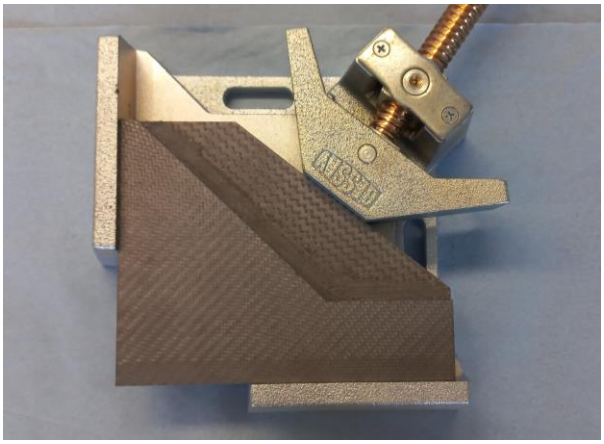

Figure 10: Joining of OCTRA40 leading edge to the remaining classical C/C-SiC part

The obtained joined component is then siliconized, yielding the impermeable classical C/C-SiC for the back component, while the leading edge becomes OCTRA40.

DOI: 10.13009/EUCASS2023-005

The fin outer contour is then milled, using diamond-based tools to machine the tenacious C/C-SiC material, and the holes for the gas feeding and for the thermocouples are obtained via electrical discharge machining (EDM).
Finally, the 6 mm stainless steel tube is soldered to the fin bottom and the thermocouples are glued in the corresponding holes with a graphite-based paste to assure thermal contact also at relatively high temperatures and with epoxy glue at the bottom to assure a stable fixture.
A picture of the fin in its final state is shown in Figure 11.

Figure 11: Fin for FinEx II.

4.2 Characterisation of the fins' overall permeability

The pressure loss of a fluid which is perfusing a porous medium can be described by the Darcy-Forchheimer equation which is formulated by Innocentini et al. [21] as with the Darcy and Forchheimer coefficients K_D and K_F as the material specific permeation properties.

$$\frac{{p_i}^2 - {p_o}^2}{2p_oL} = \left(\frac{\mu}{K_D}\right)u_D + \left(\frac{\rho}{K_F}\right){u_D}^2 \tag{12}$$

The superficial Darcy velocity u_D can be derived from the coolant mass flow rate via the continuity equation

$$u_D = \frac{\dot{m}_c}{\rho_c A_c} \tag{13}$$

In order to characterize the through-flow behaviour of the transpiration cooled fins, the permeability of the fins was determined at the AORTA (Advanced Outflow Research Facility for Transpiration Application) facility at DLR-BT [20]. Steady state pressure measurements were conducted using different mass flow rates of nitrogen at ambient temperature to obtain the pressure loss-mass flow curve. K_D and K_F were obtained by fitting the measured data according to Eq. (12), using a "least squares" algorithm. The uncertainties are determined using a Monte-Carlo method with a sample size of 200000. The resulting Darcy and Forchheimer coefficients determined for both transpiration cooled fins C1 and C2 with their respective uncertainties are given in Table 2.
As comparison K_D and K_F for the OCTRA40 determined from cylindrical samples are also given. The deviation between the values of the coefficients obtained for the fins and the plate can partially be attributed to the complex fin geometry and the corresponding uncertainty in the determination of the projected outflow area and thickness of the porous medium, which was assumed as A_c = 130 mm² and L = 25 mm as average thickness.

Table 2: Darcy and Forchheimer Coefficients of the transpiration cooled fins

	Unit	Fin C1	Fin C2	OCTRA40 Sample [13]
Darcy coefficient K_D	m²	4,89 x 10^{-12}	4,35 x 10^{-12}	1,62 x 10^{-12}
±		5,68 x 10^{-13}	4,49 x 10^{-13}	
Forchheimer coefficient K_F	m	2,59 x 10^{-7}	2,75 x 10^{-7}	4,5 x 10^{-7}
±		1,78 x 10^{-8}	2,01 x 10^{-8}	

DOI: 10.13009/EUCASS2023-005

4.3 NISI3D calibration

For the NISI3D calibration the surface of the fins had to be discretized into segments. Figure 6 depicts the applied discretization. The number of segments corresponds to the number of temperate measurements. The fins are equipped with three thermocouples each, so a total of three areas per fin can be calibrated. Since the highest heat flux is expected near the sharp leading edge, the focus is on the resolution of this area. Additionally, thermal conduction between the C/C-SiC and the OCTRA40 part can be neglected within the measurement time of the system. Therfore, the three areas are discretized solely on the OCTRA40 leading edge. All areas have the same height of 33 mm and span from the leading edge to the end of the OCTRA40 part.
The experimental setup for the NISI calibration is shown in Figure 12. The laser beam is spread homogeneously into a squared spot on the fin. The optical power is calculated from the demand voltage using the manufacturer's specifications. The laser (Laserline LDM 500-100) provides a wavelength of 910 nm. The final heat flux on the fin can then be calculated using the optical power of the laser, the area of the laser spot and the emissivity of OCTRA40. The temperatures and optical power are recorded using an oscilloscope (LeCroy WaveSurver 24 Xs-A).
A set of laser pulses is applied to one segment, which causes a temperature response at all thermocouple locations. This is done for all three segments. The surface heat flux and the temperature response are linked as described in section 2.4. A system identification procedure is then used to find all impulse responses. Each fin is a system of nine impulse responses, connecting all segments to each thermocouple.
Additionally, all fins were calibrated with the described methodology with and without cooling. The mass flow controller is the same as presented in subsection 2.2. Fin C2 was calibrated in 0.1 g/s mass flow intervals up to 1 g/s to account for the varying mass flow rate during the mission.
To further illustrate the output of the calibration an exemplary set of impulse responses is presented in Figure 13.

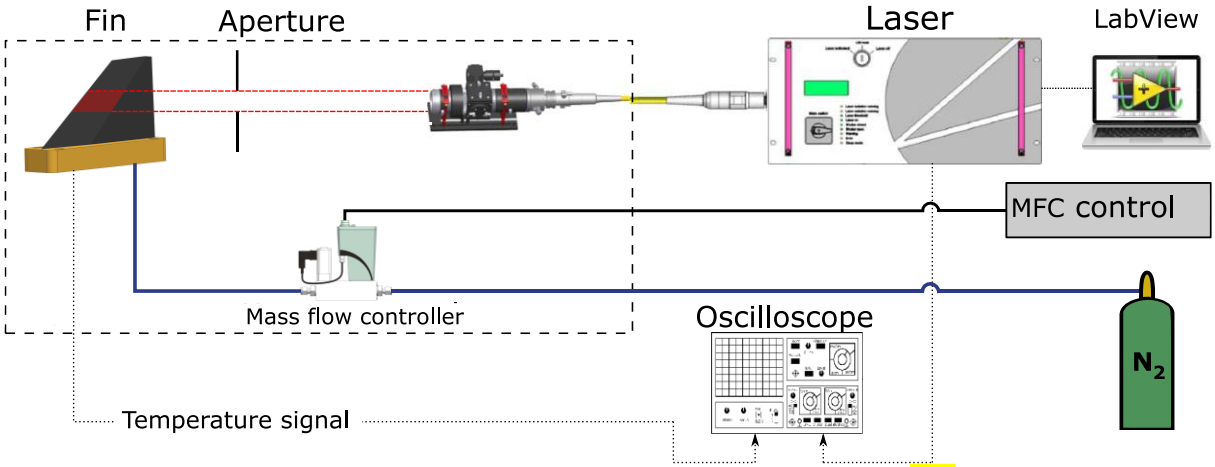

Figure 12: Experimental setup for NISI calibration (adapted from [19])

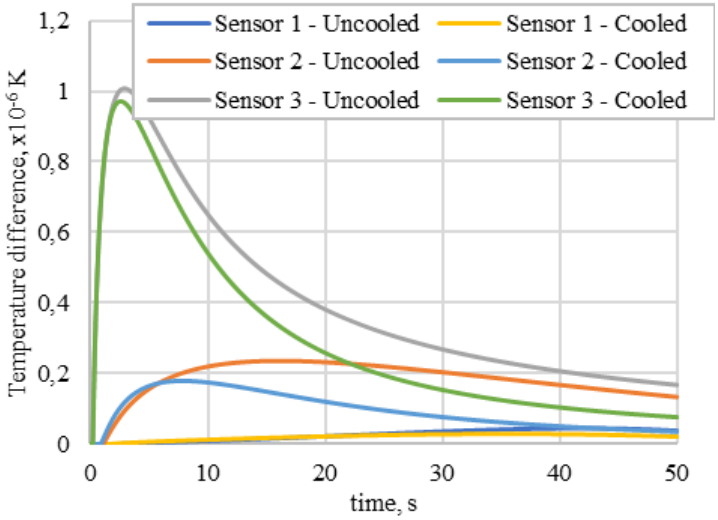

Figure 13: Sensors responses of fin C1 for impulse heat flux input the area 3.

DOI: 10.13009/EUCASS2023-005

The impulse responses are calculated for the fin C1 on the area 3 with and without cooling. The impulse response for the thermocouple closest to area 3 (sensor 3) has the strongest and fastest reaction to the incoming heat flux. Then the reaction speed and magnitude drop steadily with increasing distance, signified by sensor 2. For sensor 1 the impulse response has an almost negligible rise. This general behaviour is expected for the fin and the thermocouples combined as a system. Addressing the impulse responses for the cooled calibration a deviation to the uncooled calibration becomes evident. The general tendency is a significant reduction of the impulse responses for longer durations. This emphasizes the need of the cooled calibration, because a trustworthy heat flux measurement needs the most accurate impulse response.
In the final step of the calibration, the impulse responses are verified on an additional independent test case. This test case is a transient triangular and gaussian heat flux in succession on each area. This case is constructed by heating each area in the initial calibration position and then superpose all results. Figure 14 shows the measured temperatures, the input and the inversely calculated heat fluxes. The agreement between the input heat flux and the inverse heat flux is good, i.e. a good set of impulse responses was found.

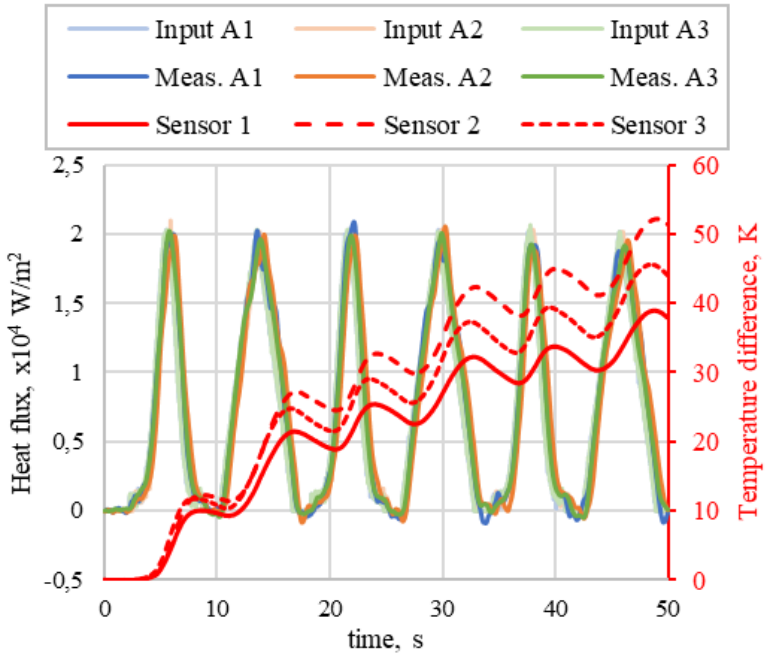

Figure 14: Impulse response verification through independent test case.

4.4 CATS calibration

The experimental setup for the CATS calibration is shown in Figure 15. The same laser system has been used for the CATS calibration as in the NISI calibration. However, the fin was oriented such that the leading edge pointed towards the optics, Mirrors on each side of the fin reflected the laser light onto both sides of the permeable part simultaneously.

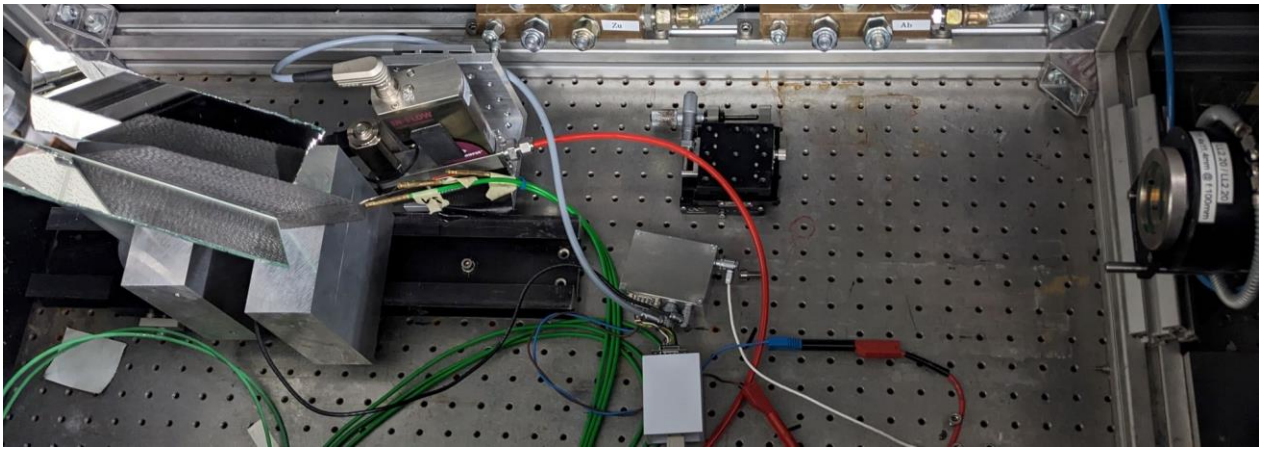

Figure 15: Experimental setup for the CATS calibration.

DOI: 10.13009/EUCASS2023-005

The actual flight hardware, including the on-board electronics box for data acquisition, all sensors, the flow controller and the gas tubing downstream of the latter, was used for the CATS calibration.
The calibration data are shown in Figure 16. The mass flow rate was set constant and the power of the calibration heat flux $\dot{q}_{cal}$ was modulated into pulses. The electronics acquired the plenum and ambient pressure (the latter remained constant at 0.89 bar) and calculated the mean fluid temperature in the porous wall and its time derivative as described in section 2.4. With these inputs, the parameters in Eq. (2) are found using a least square fit. The resulting heat flux curve $\dot{q}_m$ is given in Figure 16, which nicely matches the input heat flux.

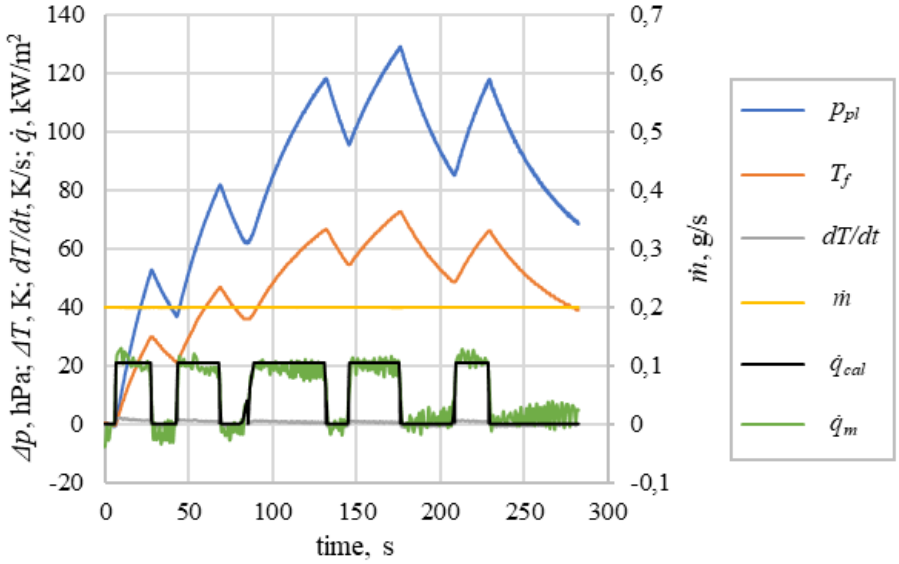

Figure 16: Calibration data set for the CATS parameter identification

The calibrated system was tested with the active CATS controller. The experimental data are given in Figure 17. Overall, the electronics determined the heat flux accurately and adjusted the mass flow rate accordingly as intended. Note, that the accurate heat flux determination is a valuable result itself.

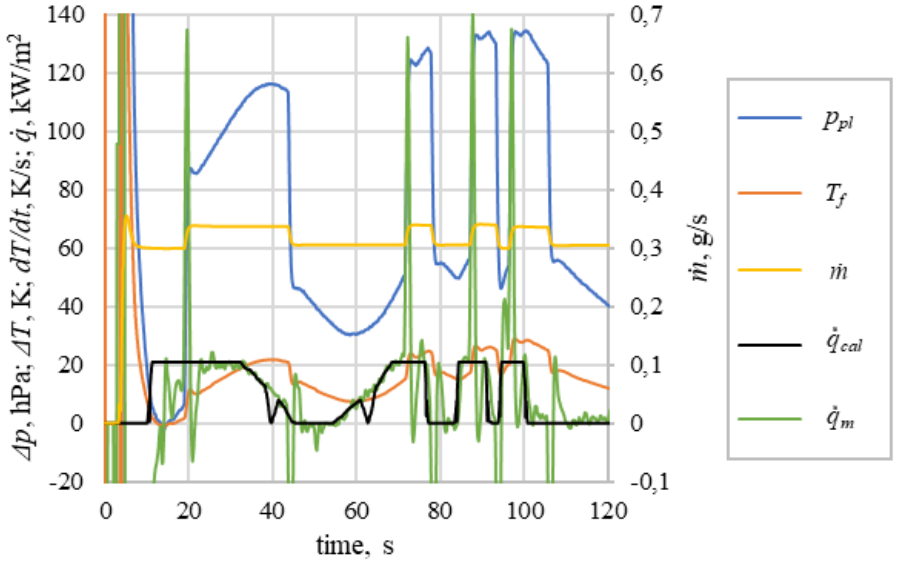

Figure 17: Qualification experiment of the active CATS controller

The heat flux measurement strongly oscillates the instant the mass flow rate is adjusted. This is due to a time delay between mass flow rate and pressure measurement caused by the utilized sensors. This oscillation was found to destabilize the controller when running at minimum cycle time of the control loop. The oscillation stabilizes after around 2 to 2,5 s. We therefore discretized the adjustment of the mass flow rate in steps of 3 s to stabilize the system. During flight, we expect at least 12 updates of the mass flow rate's setpoint for both the up- and down leg. This allows the assessment whether the system performs as intended.

DOI: 10.13009/EUCASS2023-005

It is worth noting that the mass flow rate increase is so low because the heat flux applied by the laser is rather small, i.e. about an order of magnitude lower than the expected peak heat flux during the flight experiment. The proportional factor k was set to 2.1 x 10^{-9} so at the expected peak heat flux of about 200 kW/m² (see Figure 7) the mass flow rate is increased by 0.4 g/s. This adds to the minimum mass flow rate of 0.3 g/s (see Eq. (3)).

4.5 FinExII module assembly

At this point, the gas feeding system was gradually assembled and leakage proof tests were carried out with a special attention to the high pressure line, verifying that no significant pressure loss would occur for a relatively long time, corresponding to the time between the last gas bottle fill up until lift-off. The tightness of the system was also tested under the vibrational load typical of the engine start. Some pictures are shown in Figure 18.

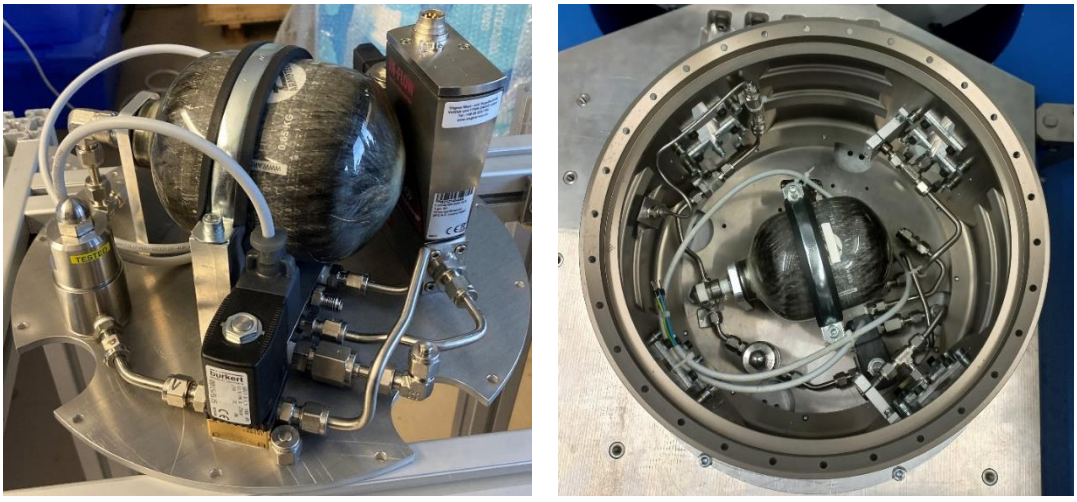

Figure 18: FinExII gas system assembly and testing.

The FinExII module was finally fully assembled, as shown in Figure 19.
In collaboration with the AFRL and DLR-MORABA, the module was then integrated with the HIFLIER1 payload, which went successfully through the bench tests, verifying the full functionality of the payload subsystems, and the environmental tests, including three different vibration tests in the under the typical loads of the engine operation.
The flight of the HIFLIER1 sounding rocket is currently scheduled in October 2023, from ESRANGE in Kiruna, Sweden.

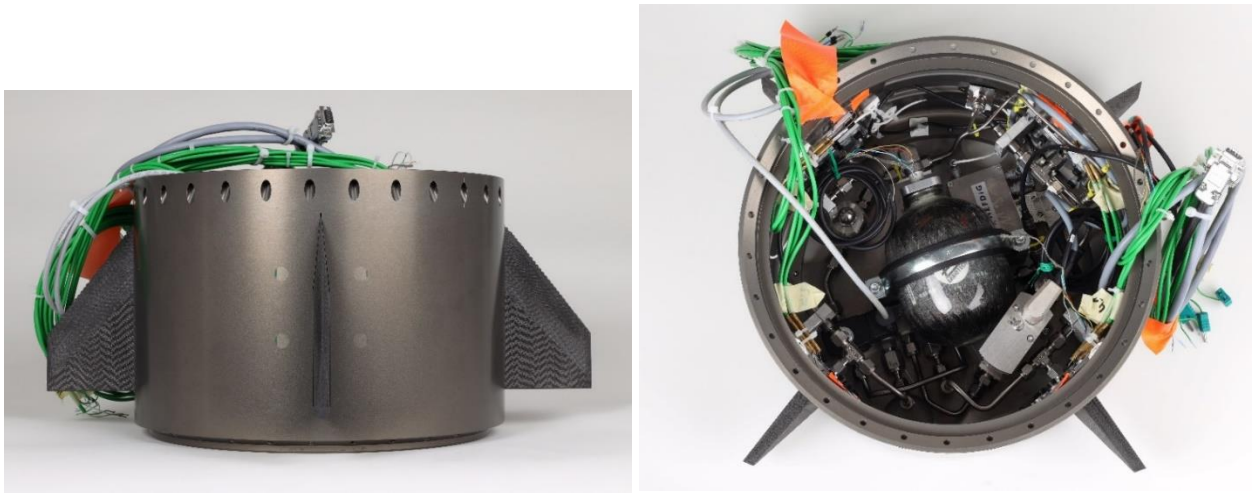

a) Side view b) Top view

Figure 19: FinEx II module fully assembled

DOI: 10.13009/EUCASS2023-005

5. Conclusions

In the framework of the HIFLIER1 flight experiment coordinated by the US Air Force Research Laboratory, DLR-BT, in collaboration with HEFDiG, is developing a module of the sounding rocket for testing the application of the transpiration cooling technology to sharp leading edges in hypersonic flight conditions.
In particular, for this application the transpiration cooling technology is combined with the use of CMC materials using a porous variant of the C/C-SiC material developed at the DLR-BT, named OCTRA40, which is employed for the leading edge of the test fins.
The design of the module, the fins and the coolant gas feeding line are described in this article. In particular, the module is instrumented with four identical fins, of which two will remain uncooled as references, while the other two will be transpiration cooled with different operating conditions. In particular, for one of the fins the CATS technique, developed by HEFDiG, for an optimized control of the coolant mass flow rate according to the actual instantaneous thermal load is implemented and tested. The effect of the transpiration cooling will be assessed by the in-depth measurements of the leading edge material temperature, which in turn will also be used for determining the spatially resolved heat flux acting on the surface by means of the so-called NISI method.
Transient thermal analyses of the CMC fin were carried out to support the design and have a first assessment of the overall effect of the transpiration cooling on the fin thermal response, considering also the case with transpiration cooling.
Finally, the pre-flight activities for the manufacturing, characterization and calibration of the fin, the verification of the gas system and the module assembly are presented.

Acknowledgments

The present work was carried out in the framework of the HIFLIER1 flight experiment project, primarily funded and coordinated by the US Air Force Research Laboratory (AFRL) und operated by DLR Mobile Rocket Base (MORABA).
Furthermore, the authors wish to thank Matthias Scheiffele and Felix Vogel from the CMC department of DLR-BT, for the manufacturing of the raw materials, and Frank Entenmann from Space System Integration department of DLR-BT for the machining of the fin and for the continuous technical support.

References

[1] Gülhan, A., Neeb, D., Thiele, T., Siebe, F. 2016. Aerothermal postflight analysis of the Sharp Edge Flight Experiment-II. *J. Spacecraft Rockets* 53:153-177. https://doi.org/10.2514/1.A33275
[2] Hald, H., Weihs, H. 2002. Safety Aspects of CMC Materials and Hot Structures. In: *Proceedings of Joint ESA-NASA Space-Flight Safety Conference*, ESA SP-486.
[3] Weihs, H., Longo, J., Gülhan, A. 2002. Sharp Edge Flight Experiment SHEFEX. In: *4th European Workshop on Thermal Protection Systems and Hot Structures Conference Proceedings*, ESA SP-521.
[4] Weihs, H., Longo, J., Turner, J. 2008. The Sharp Edge Flight Experiment SHEFEX II, a Mission Overview and Status. In: *15th AIAA International Space Planes and Hypersonic Systems and Technologies Conference*, AIAA 2008-254. https://doi.org/10.2514/6.2008-2542
[5] Gülhan, A., Hargarten, D., Zurkaulen, M., Klingenberg, F., Siebe, F., Willems, S., Di Martino, G., Reimer, T. 2023. Selected results of the hypersonic flight experiment STORT. *Acta Astronaut.*, 211:333-343. https://doi.org/10.1016/j.actaastro.2023.06.034
[6] Reimer, T., Di Martino, G., Petkov, I., Dauth, L., Baier, L., Gülhan, A., Klingenberg, F., Hargarten, D. 2023. Design, Manufacturing and Assembly of the STORT Hypersonic Flight Experiment Thermal Protection System. In: *25th AIAA International Space Planes and Hypersonic Systems and Technologies Conference*, AIAA 2023-3089. https://doi.org/10.2514/6.2023-3089
[7] Böhrk, H., Loehle, S., Fuchs, U., Elsäßer, H., Weihs, H. 2011. FinEx – Fin Experiment on HIFiRE-5. In: *7th Symposium on Aerothermodynamics for Space Vehicles*.
[8] Kays, W.M. 1972. Heat transfer to the transpired turbulent boundary layer. *Int. J. Heat Mass Transf.*, 15(5):1023–1044.
[9] Glass, D.E., Dilley, A.D., and Kelly, H.N. 2001. Numerical analysis of convection/transpiration cooling. *J. Spacecrafts Rockets*, 38(1):15–20.
[10] Dittert, C., Kütemeyer, C. 2017 Octra - Optimized Ceramic for Hypersonic Application with Transpiration Cooling, *Ceram. Transactions* 263:389-399.
[11] Dittert, C., Böhrk, H., Loehle, S. 2018. A Transpiration Cooled Wedge with adapted Permeability. In: *HiSST: International Conference on High-Speed Vehicle Science Technology*, 26.-29. Nov. 2018, Moscow, Russia.

DOI: 10.13009/EUCASS2023-005

[12] Peichl, J., Schwab, A., Selzer, M., Böhrk, H., von Wolfersdorf, J., 2022. Experimental Investigation of Transpiration Cooling in a Subscale Combustion Chamber with Non-Reactive Flow. In: *2nd International Conference on High-Speed Vehicle Science & Technology*, 12.-15. Sept. 2022, Bruges, Belgium.

[13] Di Martino, G.D., Böhrk, H., Joelle, S., Müller, C., Peichl, J., Hufgard, F., Duernhofer, C., Loehle, S. 2022. Design of the Transpiration Cooled Fin Experiment FinEx II on HIFLIER1. In: *2nd International Conference on High-Speed Vehicle Science Technology*.

[14] Böhrk, H. 2014. Transpiration cooling at hypersonic flight – AKTiV on SHEFEX II. In: *11th AIAA/ASME Joint Thermophysics and Heat Transfer Conference*, AIAA 2014-2676.

[15] Hufgard, F., Duernhofer, C., Loehle, S., Schweikert, S., Müller, C., Di Martino, G., Böhrk, H., Steelant, J., Fasoulas, S. 2022. Adjusting Transpiration Cooling to Real Time Surface Heat Flux Estimation. In: *2nd International Conference on High-Speed Vehicle Science Technology*.

[16] Loehle, S. 2017. Derivation of the non-integer system identification method for the adiabatic boundary condition using Laplace transform. *Int. J. of Heat and Mass Transf.*, 115:1144-1149. https://doi.org/10.1016/j.ijheatmasstransfer.2017.08.007

[17] Beck, J.V., Blackwell, B., St. Clair Jr., C.R. 1985. Inverse Heat Conduction: Ill-posed Problems. John Wiley & Sons, Inc., New York.

[18] Duernhofer, C., Hufgard, F., Fasoulas, S., Loehle, S. 2022. Investigation of Spatially Resolved Heat Flux Determination from In-Depth Temperature Data. In: *2nd International Conference on Flight Vehicles, Aerothermodynamics and Re-entry Missions & Engineering (FAR)*.

[19] Müller, C. 2022. Investigation of the thermal behavior of a transpiration-cooled ceramic fin for HIFLIER1 with inverse heat conduction methods. Master's thesis. University of Stuttgart, Institute of Space Systems, IRS-22-S-035.

[20] Peichl, J., Schwab. A., Selzer, M., Böhrk, H., van Wolfersdorf, J. 2021. Innovative Cooling for Rocket Combustion Chambers. In: Future Space-Transport-System Components under High Thermal and Mechanical Loads Notes on Numerical Fluid Mechanics and Multidisciplinary Design (146). Springer Nature. Cham, Switzerland.

[21] Innocentini, M.D.M., Nascimento L.A., Pandolfelli, V.C. 2004. The pressure-decay technique for air permeability evalulation of dense refactory ceramics. *Cement and Concrete Research* 34:293-298. https://doi.org/10.1016/j.cemconres.2003.08.006